Wavefront sensor architectures fully embedded in an image sensor

Jérôme Vaillant

Wavefront sensor architectures fully embedded in an image sensor

Jérôme Vaillant

STMicroelectronics, 850 rue Jean Monnet, 38920 Crolles, France

jerome.vaillant@st.com

Several architectures of wavefront sensors have been developed since the rise of adaptive optics. In all cases, optical elements are placed in front of image sensors. This makes the sensor quite bulky, expensive, and sensitive to optical misalignment. I propose two novel architectures fully embedded in the image sensor that require no additional optical element. The sensor can be placed directly in the beam to analyze, leading to small, easy to use, and cost-efficient systems. The two architectures are described before testing by simulation of their ability to sense the wavefront distortion and their sensitivity to signal-to-noise ratio.

1. Introduction

Wavefront sensing technique has been developed by astronomers for adaptive optics [1] to compensate for the degradation of image resolution due to atmospheric turbulence. That method is now used in other fields such as laser optics [2,3] for beam shape characterization, ophthalmology [4–6] for eye aberrations correction (low light eye examination or laser surgery), or thin film metrology [7]. In all these applications the key tool is the wavefront sensor. Several architectures have been proposed [8,9]. But all these sensors require optical elements (such as a microlens array, shearing plate, or pyramidal prism) and an image sensor, making their use expensive and requiring optical alignment of the system. Some recent efforts have been done to develop a cost-effective Shack–Hartmann wavefront sensor [10–12] using low-cost devices such as complementary metal-oxide semiconductor (CMOS) image sensors instead of charge-coupled device (CCD) ones, but the additional optical elements remain mandatory.These elements can be suppressed with thet wo novel architectures proposed in this paper: the wavefront is sensed directly on the image sensor.

A general view of the image sensor pixel architecture is given in Section 2, providing the required background for the architectures development. Then the two proposed architectures, called “embedded Shack–Hartmann” (eSH) and “embedded quad cells” (eQC) sensors are presented in Section 3. For each architecture, the performances are estimated by simulating the devices in Section 4. Finally, these performances are compared, and the possibilities of application are investigated in Section 5.

2. Pixel Architecture of Image Sensor

The concepts of the two embedded wavefront sensors are applicable to any kind of image sensor whose photosensitive area is smaller than the pixel itself. This paper deals with the CMOS image sensors that nowadays present comparable performances to CCD [13–17]. However, CCD image sensors can be used if the photosensitive area is smaller than the pixel.

A CMOS image sensor differs from a CCD one by the presence of an active part inside all pixels ensuring the functions of reset, readout, and addressing (for detailed introduction to CMOS image sensors see [16]). These active pixels require three transistors (respectively denoted as RST for reset, RD for readout, and ADD for addressing). Better noise performances are achieved by correlated double sampling (CDS) and introduction of a fourth transistor denoted TG for transfer gate [see Fig. 1(a)]. This will geometrically reduce the size of the photosensitive area relative to pixel size (or fill factor), as seen on the pixel layout in Fig. 1(b).

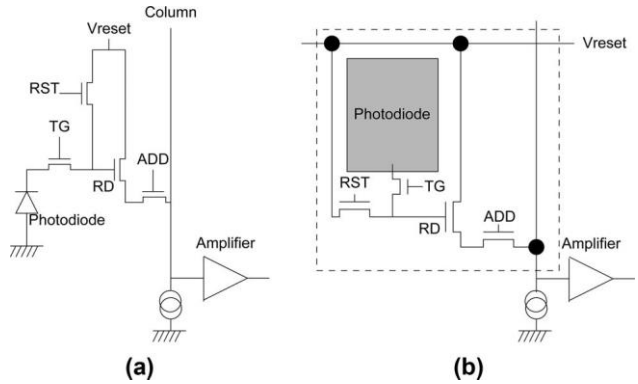

Fig. 1. (a) Schematic and (b) layout of a standard four transistors CMOS pixel.

This geometrical loss is customarily compensated by placing a microlens on top of each pixel [18,19]: it concentrates the

light to the photosensitive area [see Fig. 2(a)]. These microlenses are processed as a final step of the image sensor production in the standard semiconductor flow. The usual process [20–22] is done on three main steps: (i) deposition of a photoresist layer over the wafer, (ii) photolithography of this resist to define the microlens footprint, and (iii) reflow of the previously defined parallelepipeds to form a resist bubble: the microlens. Thus microlens footprints are controlled by mask design, and a resolution as low as 5 nm is easily achievable. Finally, the microlenses placement with respect to the pixel depends on the photolithography accuracy and can be maintained lower than 50 nm with standard CMOS industry tools.

These microlenses, usually placed on top of each pixel, are designed [23] and positioned to maximize the output signal of the pixel: under normal incidence, the optical axis of a microlens is aligned with the center of the photosensitive area [see Fig. 2(a)]. Under oblique incidence it can be shifted to center the focal point on the photosensitive area [see Fig. 2(b)]. For a pixel located on the edge of the array for a sensor (placed behind an objective lens), the microlens is shifted toward the center of the pixel array.

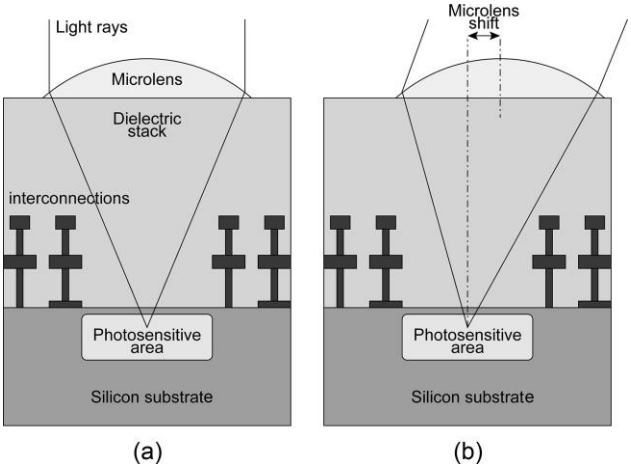

Fig. 2. Vertical cut of a standard CMOS pixel (a) under normal incidence and (b) under oblique incidence.

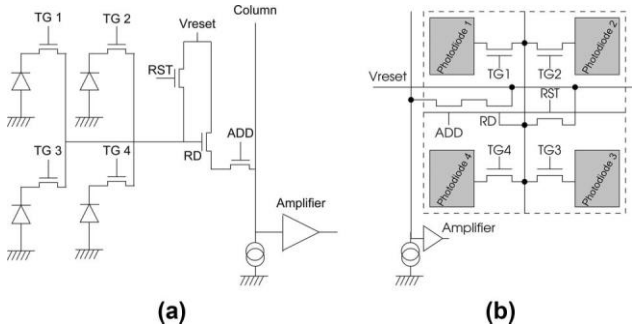

Fig. 3. (a) Schematic and (b) layout of a standard "1.75" transistor CMOS pixel. Typical offset of the photodiodes on shared architecture is shown as a layout view; here 2 2 pixels are represented.

This shift is simply done by shrinking the microlens matrix compared to the pixel array at design level, for instance by defining a microlens footprint with a pitch slightly smaller than the pixel one. It can also be interesting to increase the microlens pitch compare to the pixel one. This is a nice way to map the intrapixel sensitivity and cross talk between pixels [24]. The eSH uses these pixel-scan patterns, providing images similar to Shack–Hartmann sensor ones, from which comes the name.

In addition, in the past decade, the size of the pixel has steeply shrunk, making it difficult to ensure reasonable photodiode size and reducing the pixel performances even with optimized microlenses. That is why shared architectures have been introduced [25,26]. In these architectures the read, reset, and addressing transistors are shared between pixels, so seven transistors are used for four pixels, leading to so-called 1.75 transistors pixel architectures [see Fig. 3(b)]. In such a design the four pixels usually have a symmetrical layout with an unbalanced photodiode placement (see Fig. 3). Under normal incidence, microlenses placed uniformly over the image array lead to balanced signals between the different pixels. Under oblique incidence, a pixel on four will be privileged, as for quad-cell detection. The eQC used this 1.75 transistor pixel asymmetry, forming a matrix of quad-cell detectors.

3.Wavefront Sensor Architectures

A. Embedded Shack–Hartmann: eSH

This sensor is made of several pixel-scan areas stitched over the whole pixel array. This divides the image sensor in analysis areas, each one providing the tilt of the wavefront over it, like a Shack–Hartmann sensor but without any additional optical part.

If each analysis area is constituted of $N \times N$ pixels, these pixels will be covered by $N-1 \times N-1$ microlens (the analysis area can have a rectangular shape in the general case, but for simplicity, a square shape is assumed). Then each microlens has a pitch a_m greater than the pixel pitch a_p, given by $a_m = a_p[1 + 1/(N-1)]$. For a sensor constituted of $M \times M$ pixels (with $M > N$), the number of wavefront sampling areas is $M/N \times M/N$. For each area, the maximum output signal is obtained for a shift δ_{max} of the microlens optical axis relative to the photodiode center equal to the shift δ_{tilt} introduced by the tilt of the wavefront (see Fig. 4):

$$\delta_{tilt} = h_{stack} \tan\left[\arcsin\left(\frac{\sin\theta_0}{n_{stack}}\right)\right] \quad (1)$$

with θ_0 the tilt of the wavefront, n_{stack} the refractive index of the dielectric stack between the microlens and the photodiode, and h_{stack} the thickness of this stack.

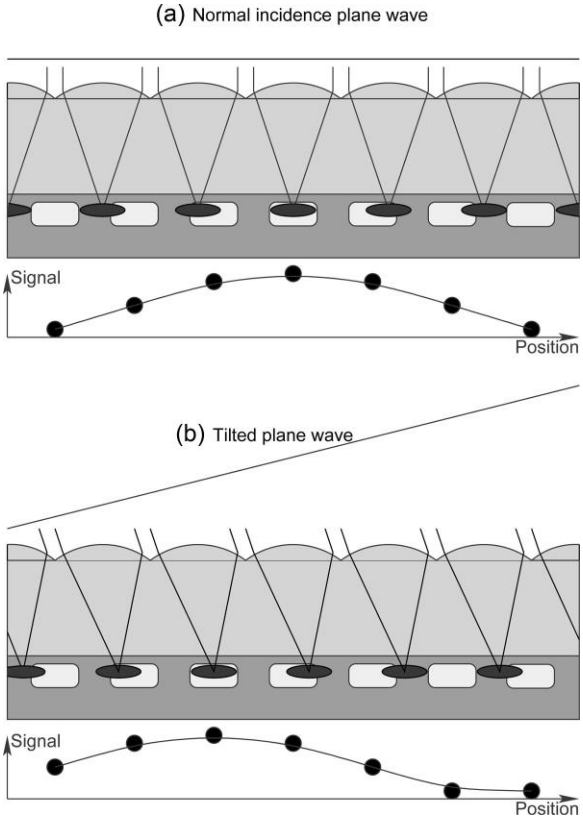

Fig. 4. eSH principle: for each analysis area the maximum of signal is obtained for a microlens shift equal to the shift introduce by the tilt of the wavefront. (a) For normal incidence plane wave the maximum is centered on the analysis area. (b) For tilted plane wave the maximum is shifted according to Eq. (1).

The determination of the signal maximum location provides the tilt on each analysis area by inverting Eq. (1). This location can be estimated by different algorithms, for instance, centroid and derivatives or polynomial fitting. In this paper we consider the maximum of the parabola fitted on each analysis area. The results obtained on simulated images are detailed in Subsection 4.A.

At this level a limitation of the present wavefront sensor appears: the tilt of the wavefront over each pixel (giving the pixel output signal) has to be correlated over the analysis area ($N \times N$ pixels). Otherwise high spatial frequencies, present in the wavefront, will lead to erroneous estimation: the shape of the intensity distribution inside an analysis area can present local maxima, making the overall tilt estimation more difficult. This error will be more complex than the alias ing error [27–29] in case of Shack–Hartmann wavefront sensor. However, this limitation can be overcome by the second architecture presented in Subsection 3.B, where the analysis area is limited to 2 2 pixels.

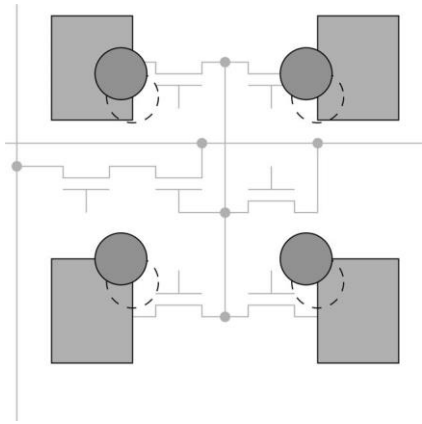

Fig. 5. eQC principle: for a normal incidence plane wave the focal spots are placed regularly at the silicon level (dashed circles), for a tilted plane wave, the spots (solid circles) displacement modifies the signal of the pixel, increasing one while decreasing the three others.

B. Embedded Quad Cells: eQC

This sensor is based on the decentering of the photosensitive area in most of the shared architectures. An advantage of the present sensor compared to the eSH is that the size of the analysis area is limited to 2×2 pixels. So the wavefront has to be correlated only over a small zone. The described architecture is based on the so-called 1.75 transistors pixel architecture. In this case the layout of the pixel is no more done unitary but for a group of four pixels sharing three transistors. They are generally placed in the center of the design, moving the photosensitive areas outward (see Fig. 3). Then placing the microlens uniformly over all pixels leads to a misalignment between their optical axis and the photosensitive area centers. When a tilted wavefront hits a 2×2 group of pixels, the focal point of the microlens is moving either toward the center of the photosensitive area, increasing the signal, or outward, decreasing the signal (see Fig. 5). This behavior is similar to a four quadrants cell and measures the gradient of the wavefront to sense.

4.Simulated Performances of Wavefront Sensor Architectures

The performances of the two architectures in terms of wavefront tilt estimation are evaluated by simulation. This is done in two steps: at first the sensitivity to pure tilt is checked; then the ability to sense a random phase map is tested. In both cases the estimation is done on noiseless images before doing it on noisy data (including photon noise

Table 1. Figures Used for Wavefront Sensor Simulation

a_p	h_{stack}	n_{stack}	λ	η	$\sigma_{readout}$	M	N	Φ
3 µm	6 µm	1.5	500 nm	50%	$5e^-$	250	25	$10^5/10^4/10^3/10^2$/ photons

at different level and readout noise). As a first step a phase screen is generated with a size of $(2M+1)\times(2M+1)$, then by simple finite differentiation, the spatial derivative of this phase map, *i.e.*, the tilt map over the sensor pixels is calculated. Finite differentiation returns a tilt map with a size of $M \times M$. Knowing this tilt and the energy distribution at the focal plane of the microlens, the signal of all pixels (*i.e.*, the image) is calculated, depending on the architecture. Here we neglect the effect of interconnections inside the dielectric stack between the microlens and the silicon to ensure an analytical model of the images.

That energy distribution is approximated by a Gaussian distribution. This assumption is driven by the fact that the pixel is small (from 2 to 10 µm for the advanced CMOS image sensor) so the shape of the spot formed by the microlens in the silicon is dominated by diffraction. With this hypothesis, the integration of the energy over the rectangular photosensitive area is made easier. The Gaussian width is chosen so that its energy equals the Airy spot energy:

$$\iint_{-\infty}^{+\infty} \exp\left[-\frac{x^2+y^2}{2\sigma^2}\right]\mathrm{d}x\mathrm{d}y = \iint_{-\infty}^{+\infty} \frac{4J_1^2\left(\sqrt{x^2+y^2}\right)}{x^2+y^2}\mathrm{d}x\mathrm{d}y$$

This gives a Gaussian width σ of

$$\sigma = \frac{32}{3\pi\sqrt{2\pi}}\frac{\lambda h_{stack}}{\pi a_p} \tag{2}$$

The amplitude of the Gaussian is given by the number of incident photons per pixel Φ and the quantum efficiency of the pixel η. So the intensity is given by

$$I(x,y) = \Phi\eta \exp\left[-\frac{x^2+y^2}{2\left(\frac{32}{3\pi\sqrt{2\pi}}\frac{\lambda h_{stack}}{\pi a_p}\right)}\right] \tag{3}$$

A detailed model for each architecture is presented in Subsections 4.A and 4.B. These models allow generation of simulated images. Then noises are added to these images. The photon shot noise follows a Poisson law with a mean equal to the signal level of each pixel of simulated images. This level is related to the overall incident flux Φ on the wavefront sensor, given in photons per pixel. The additive readout noise follows a centered Gaussian law with a variance $\sigma^2_{readout}$. Finally, the performances are compared in Subsection 4.C. All simulations are done using the figures given in Table 1.

A. Embedded Shack–Hartmann Wavefront Sensor

The eSH sensor is simulated assuming a photosensitive area centered on the pixel with a size of $(1/2)a_p \times (1/2)a_p$. This parameter can easily be controlled by a proper pixel design and tune depending on the trade-off between low light sensitivity and tilt sensitivity: the smaller the photosensitive area, the greater the tilt sensitivity. The simulated image is generated by the following steps:

1. For each pixel (i,j) of the sensor, the shift in the *x* and *y* directions (due to the tip-tilt of the phase over that pixel) is calculated using Eq. (1). They will be denoted $\delta^x_{tilt}(i,j)$ and $\delta^y_{tilt}(i,j)$, respectively.
2. For each pixel (i,j) of the sensor, the shift of the microlens optical axis in *x* and *y* directions is calculated, depending on the pixel coordinates (i,j):

$$\delta^x_\mu(i,j) = a_p\left[\mathrm{Frac}\left(\frac{i}{N}\right)-\frac{1}{2}\right]$$
$$\delta^y_\mu(i,j) = a_p\left[\mathrm{Frac}\left(\frac{j}{N}\right)-\frac{1}{2}\right] \tag{4}$$

with Frac (*x*) denoting the fractional part of *x*.

3. The output signal of the pixel i, j is obtained by integration of the Gaussian distribution, using the erf function

$$\begin{aligned} S(i,j) = &\int_{-\frac{a_p}{2}+\delta^x_{tilt}(i,j)+\delta^x_\mu(i,j)}^{\frac{a_p}{2}+\delta^x_{tilt}(i,j)+\delta^x_\mu(i,j)}\int_{-\frac{a_p}{2}+\delta^y_{tilt}(i,j)+\delta^y_\mu(i,j)}^{\frac{a_p}{2}+\delta^y_{tilt}(i,j)+\delta^y_\mu(i,j)} \Phi\eta \\ &\times \exp\left[-\frac{x^2+y^2}{2\left(\frac{32}{3\pi\sqrt{2\pi}}\frac{\lambda h_{stack}}{\pi a_p}\right)}\right]\mathrm{d}x\mathrm{d}y \\ = \Phi\eta &\left[\mathrm{erf}\left(\frac{\frac{a_p}{2}+\delta^x_{tilt}(i,j)+\delta^x_\mu(i,j)}{\frac{32}{3\pi\sqrt{2\pi}}\frac{\lambda h_{stack}}{\pi a_p}}\right) - \mathrm{erf}\left(\frac{-\frac{a_p}{2}+\delta^x_{tilt}(i,j)+\delta^x_\mu(i,j)}{\frac{32}{3\pi\sqrt{2\pi}}\frac{\lambda h_{stack}}{\pi a_p}}\right)\right] \\ &\times\left[\mathrm{erf}\left(\frac{\frac{a_p}{2}+\delta^y_{tilt}(i,j)+\delta^y_\mu(i,j)}{\frac{32}{3\pi\sqrt{2\pi}}\frac{\lambda h_{stack}}{\pi a_p}}\right) - \mathrm{erf}\left(\frac{-\frac{a_p}{2}+\delta^y_{tilt}(i,j)+\delta^y_\mu(i,j)}{\frac{32}{3\pi\sqrt{2\pi}}\frac{\lambda h_{stack}}{\pi a_p}}\right)\right] \end{aligned} \tag{5}$$

The reference output image (i.e., the response to a plane wave under normal incidence) is shown in Fig. 6. On this simulated image, two sources of noise are added: photon noise following the Poisson law and sensor overall noise following a Gaussian law. The estimated tilt is given by the location of the signal maximum. This is evaluated by fitting a parabola on threshold subimages. Each subimage

corresponds to a pixel-scan area, and only pixels having an intensity greater than 80% of the maximum are used. This thresholding makes the estimation more stable at low signal-to-noise ratio.

B. Embedded Quad Cells Wavefront Sensor

To simulate this sensor, the microlens pitch is set equal to the pixel pitch: $a_m = a_p$. So there are no $\delta_\mu^x(i,j)$ and $\delta_\mu^y(i,j)$. But the photosensitive areas are decentered (by δ_{ph}^x and δ_{ph}^y along the x and y axes), depending on the parity of the pixel coordinates:

$$\delta_{ph}^x(i,j) = \begin{cases} -0.2a_p & \text{if } i \text{ is even} \\ +0.2a_p & \text{if } i \text{ is odd} \end{cases}$$

$$\delta_{ph}^y(i,j) = \begin{cases} -0.2a_p & \text{if } j \text{ is even} \\ +0.2a_p & \text{if } j \text{ is odd} \end{cases} \quad (6)$$

This decentering is taken equal to $0.2a_p$. Then the output signal of a pixel i, j is given by:

$$\begin{aligned} S(i,j) = & \int_{-\frac{a_p}{2}+\delta_{ph}^x(i,j)}^{\frac{a_p}{2}+\delta_{ph}^x(i,j)} \int_{-\frac{a_p}{2}+\delta_{ph}^y(i,j)}^{\frac{a_p}{2}+\delta_{ph}^y(i,j)} \Phi\eta \\ & \times \exp\left[-\frac{x^2+y^2}{2\left(\frac{32}{3\pi\sqrt{2\pi}}\frac{\lambda h_{stack}}{\pi a_p}\right)}\right] \mathrm{d}x\mathrm{d}y \\ = \Phi\eta & \left[\mathrm{erf}\left(\frac{\frac{a_p}{2}+\delta_{ph}^x(i,j)}{\frac{32}{3\pi\sqrt{2\pi}}\frac{\lambda h_{stack}}{\pi a_p}}\right) - \mathrm{erf}\left(\frac{-\frac{a_p}{2}+\delta_{ph}^x(i,j)}{\frac{32}{3\pi\sqrt{2\pi}}\frac{\lambda h_{stack}}{\pi a_p}}\right)\right] \\ & \times \left[\mathrm{erf}\left(\frac{\frac{a_p}{2}+\delta_{ph}^y(i,j)}{\frac{32}{3\pi\sqrt{2\pi}}\frac{\lambda h_{stack}}{\pi a_p}}\right) - \mathrm{erf}\left(\frac{-\frac{a_p}{2}+\delta_{ph}^y(i,j)}{\frac{32}{3\pi\sqrt{2\pi}}\frac{\lambda h_{stack}}{\pi a_p}}\right)\right] \end{aligned} \quad (7)$$

The tilt is estimated by calculating the centroid on the 2×2 pixels. This function is not linear with the tilt but shows good sensitivity. Here it is interesting to note that the energy distribution on the focal plane of the microlens is mainly determined by the diffraction of the light by the microlens (a few micrometers wide). But, because the sampling of the wavefront is also done at microlens pitch, this diffraction effect does not impact the sensed image(or, more precisely, not more than it does on the CMOS sensor used for any other application). So the eQC is not (or slightly) impacted by the wavefront variation over a pixel, canceling the usual centroid gain variation [30] in a quad-cell detection system.

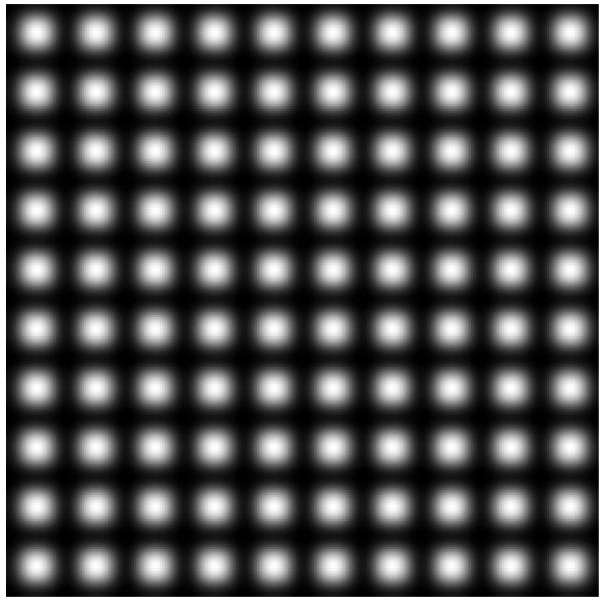

Fig. 6. Response of the eSH wavefront sensor to a plane wave.

C. Performances

At first the sensitivity to pure tilt is checked, showing good results for angles up to 0.2 rad. The results are summarized in Table 2. Figures 7(a) and 7(b) show, respectively, the response of the eSH and the eQC sensors to pure tilt between 0 rad and 0.2 rad for number of incident photons of 10^2 and readout noise of $\sigma_{readout} = 5e^-$. The error bars indicate $\pm 3\sigma$ dispersion of measurement over the whole sensor. One can note the maximum rms errors for both architectures are achieved for a tilt of 0.2 rad and are quite similar. However, eSH shows better performances for all other tilts (smaller error bars on Fig. 7), thanks to a larger number of pixels used to estimate the tilt: this averages the noise over tens of pixels instead of simply four in the case of eQC sensor.

Table 2. Maximum rms Error on Tilt Estimation between 0 rad and 0.20 rad

Level of Signal (ph/pixel)	eSH max rms Error [rad]	eQC max rms Error [rad]
10^5	37×10^{-6}	43×10^{-6}
10^4	107×10^{-6}	131×10^{-6}
10^3	229×10^{-6}	407×10^{-6}
10^2	1.35×10^{-3}	1.32×10^{-3}

A more realistic case has been studied using a random phase screen (see Fig. 8). The rms error on tilt estimation over the sensor is given in Table 3. The phase map is the projection of a Kolmogorov wavefront [31] on the first 45 components of a modal basis. These modes are constructed using a polynomial on Cartesian coordinates up to the eighth order and orthogonalization.

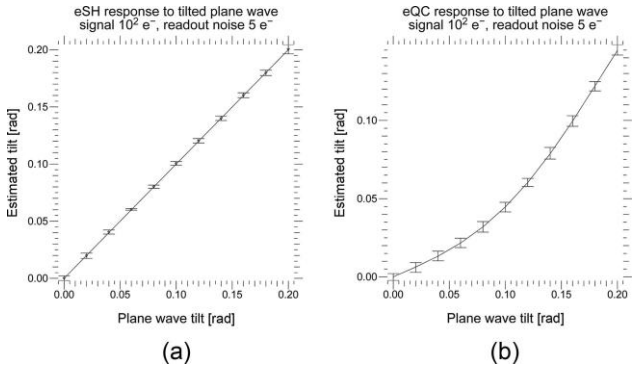

Fig. 7. Sensitivity of (a) eSH and (b) eQC wavefront sensors to tilted plane wave.

The support of each polynomial has a square shape and its size is $(2M+1)\times(2M+1)$; see Fig. 9. This random phase has a max tilt value of 97×10^{-3} rad, a minimum tilt value of 132×10^{-3} rad, and an overall rms tilt value of 7×10^{-3}rad.

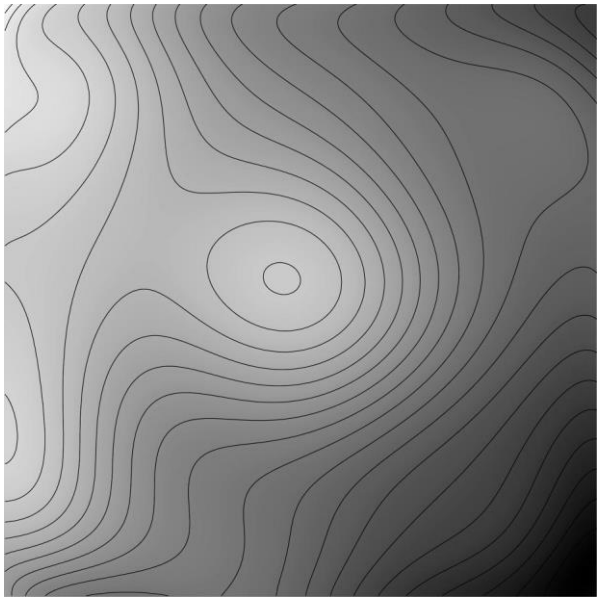

Fig. 8. Random wavefront used for eSH and eQC performances analysis.

Table 3. rms Error on Local Tilt Estimation of Random Wavefront

Level of Signal	eSH rms Error [rad]	eQC rms Error [rad]
10^5 ph/pixel	35×10^{-6}	36×10^{-6}
10^4 ph/pixel	132×10^{-6}	37×10^{-6}
10^3 ph/pixel	360×10^{-6}	110×10^{-6}
10^2 ph/pixel	461×10^{-6}	300×10^{-6}

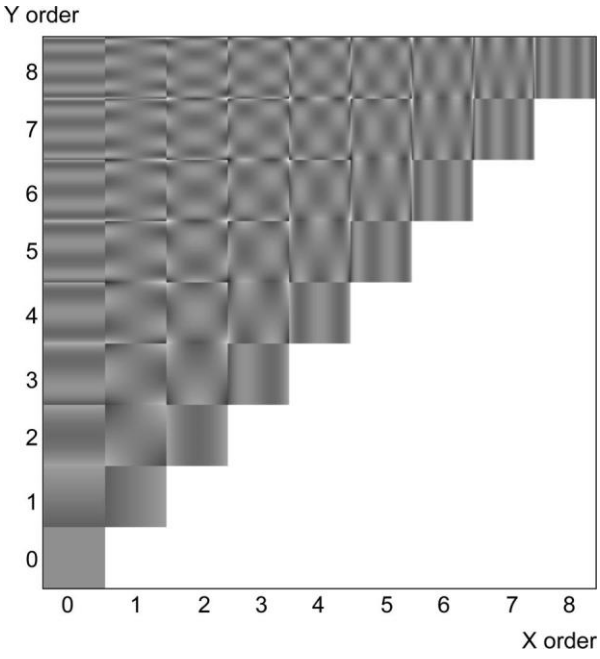

Fig. 9. Basis used to construct random phase screens.

5. Conclusion

The two architectures presented in this paper are unique solutions to make optic-less wavefront sensors: the embedded Shack–Hartmann (eSH) and the embedded quad cells (eQC). They take advantage of two features of advanced image sensor architecture: microlenses are customarily placed on top of each pixel, and the the photosensitive area of the pixel is smaller than the pixel itself. Then little modifications of the image sensor design (control of the photosensitive area and microlens pitch) turn a classic image sensor into an integrated wavefront sensor. This induces several advantages leading to compact, robust, and cheap wavefront sensors: these wavefront sensors can be placed directly on the beam to analyze, they require no external or additional optical system, and they can be produced without any extra fabrication cost. Also by using CMOS technology, it is possible to embed the signal processing inside the die, and to use the high frame rate now available on these image sensors. CMOS image sensors also allow random access to the pixel; then it is possible to define dynamically the shape of the detection, making the sensor very versatile. It is possible to make it consistent with the optical pupil of the system, for instance, hexagonal shape or central obstruction.

After the description of the two proposed architectures, their performances have been checked in terms of pure wavefront deformation. At first the sensitivity of such sensors to a tilted plane wave have been studied. Both architectures have shown good performances even with quite low signal-to-noise ratio. Then the ability to sense a complex wavefront has been checked. This exhibits a limitation for the eSH

architecture: the wavefront has to be smooth over the analysis area; the wavefront is not filtered by any optic. This limitation can be strongly reduced with the eQC architecture where the analysis area is only 2×2 pixels. In this paper, focused on architecture description and wavefront sensing ability, the local wavefront tilt is determined using simple and easy to implement algorithms. For the eSH the local tilt is calculated from the position of the maximum of the parabola fitted on each subimage. For the eQC, tilt estimation used the classical quad-cell centroid. Further evaluation of these architectures will involve a centered comparison with the already available wavefront sensors such as Shack–Hartmann, curvature, or pyramidal ones. This will require a deeper study of signal processing and wavefront reconstruction to determine the optimal algorithm for each architecture. Realistic cases must also be taken into account, such as scintillation (in weak or strong regime), and finally the implementation on a real chip will allow characterization of this wavefront sensor. It will also be interesting to tune the pixel architecture and microlens placement to meet the needs. For instance, we could privilegate the sensitivity for low light level (with large pixel size) or high sensitivity to local tilt (with a smaller photosensitive area compared to the pixel surface).

References

1. M. C. Roggemann and B. M. Welsh, *Imaging Through Turbulence* (CRC Press, 1996).
2. D. R. Neal, W. J. Alford, J. K. Gruetzner, and M. E. Warren,"Amplitude and phase beam characterization using a twodimensional wavefront sensor," Proc. SPIE **2870,** 72–82 (1996).
3. J. D. Mansell, J. Hennawi, E. K. Gustafson, M. M. Fejer, R. L.Byer, D. Clubley, S. Yoshida, and D. H. Reitze, "Evaluating the effect of transmissive optic thermal lensing on laser beam quality with a Shack–Hartmann wavefront sensor," Appl. Opt. **40,** 366–374 (2001).
4. D. Merino, C. Dainty, A. Bradu, and A. G. Podoleanu, "Adaptive optics enhanced simultaneous en-face optical coherence tomography and scanning laser ophthalmoscopy," Opt. Express **14,** 3345–3353 (2006).
5. F. Díaz–Doutón, J. Pujol, M. Arjona, and S. O. Luque, "Curvature sensor for ocular wavefront measurement," Opt. Lett. **31,** 2245–2247 (2006).
6. S. R. Chamot, C. Dainty, and S. Esposito, "Adaptive optics forophthalmic applications using a pyramid wavefront sensor," Opt. Express **14,** 518–526 (2006).
7. C. R. Forest, C. R. Canizares, D. R. Neal, M. McGuirk, andM. L. Schattenburg, "Metrology of thin transparent optics using Shack–Hartmann wavefront sensing," Opt. Eng. **43,** 742– 753 (2004).
8. F. Rigaut, B. L. Ellerbroek, and M. J. Northcott, "Comparisonof curvature-based and Shack–Hartmann-based adaptive optics for the Gemini telescope," Appl. Opt. **36,** 2856–2868 (1997).
9. T. Y. Chew, R. M. Clare, and R. G. Lane, "A comparison of theShack–Hartmann and pyramid wavefront sensors," Opt. Commun. **268,** 189–195 (2006).
10. J. D. Mansell, P. B. Catrysse, E. K. Gustafson, and R. L. Byer,"Silicon deformable mirrors and CMOS-based wavefront sensors," Proc. SPIE **4124,** 15–25 (2000).
11. D. W. de Lima Monteiro, G. Vdovin, and P. M. Sarro, "Highspeed wavefront sensor compatible with standard CMOS technology," Sens. Actuators A **109,** 220–230 (2004).
12. O. La Schiazza, T. Nirmaier, M. Han, and J. Bille, "A customCMOS-based Hartmann–Shack wavefront sensor," Invest. Ophthalmol. Visual Sci. **46,** 2002–B771 (2005).
13. E. R. Fossum, "Active pixel sensors: are CCDs dinosaurs?"Proc. SPIE **1900,** 2–14 (1993).
14. E. Fossum, "CMOS image sensors: electronic camera-on-achip," IEEE Trans. Electron. Devices **44,** 1689–1698 (1997).
15. S. U. Ay, M. P. Lesser, and E. R. Fossum, "CMOS active pixelsensor (APS) imager for scientific applications," Proc. SPIE **4836,** 271–278 (2002).
16. A. El Gamal and H. Eltoukhy, "CMOS image sensors: an introduction to the technology, design, and performance limits, presenting recent developments and future directions," IEEE Circuits Devices Mag. **21**(3), 6–20 (2005).
17. M. Bigas, E. Cabruja, J. Forest, and J. Salvi, "Review of CMOSimage sensors," Microelectron. J. **37,** 433–451 (2006).
18. M. Deguchi, T. Maruyama, F. Yamasaki, T. Hamamoto, and A.Izumi, "Microlens design using simulation program for CCD image sensor," IEEE Trans. Consumer Electronics **38,** 583– 589 (1992).
19. S. U. Lee, J. L. Park, J. S. Choi, and J. G. Lee, "The fabricationprocess and characteristics of light loss free zero-space microlenses for CMOS image sensor," Proc. SPIE **5754,** 1241–1248 (2005).
20. Y.–T. Fan, C.–S. Peng, and C.–Y. Chu, "Advanced microlensand color filter process technology for the high-efficiency CMOS and CCD image sensors," Proc. SPIE **4115,** 263–274 (2000).
21. H.–J. Hsu, F.–T. Weng, C.–K. Chang, and Y.–K. Hsiao,"Microlens design for compact lens system," Proc. SPIE **5116,** 640–646 (2003).
22. D. A. Baillie and J. E. Gendler, "Zero-space microlenses forCMOS image sensors: optical modeling and lithographic process development," Proc. SPIE **5377,** 953–959 (2004).
23. J. Vaillant and F. Hirigoyen, "Optical simulation for CMOSimager microlens optimization," Proc. SPIE **5459,** 200–210 (2004).
24. G. Agranov, V. Berezin, and R. H. Tsai, "Cross talk and microlens study in color CMOS image sensor," IEEE Trans. Electron. Devices **50,** 4–11 (2003).
25. M. Mori, M. Katsuno, S. Kasuga, T. Murata, T. Yamaguchi, M.Ind, and J. Kyoto, "A 14 in. 2M pixel CMOS image sensor with 1.75 transistorpixel," *Dig. Tech. Pap.-IEEE Int. Solid-State Circuits Conf.* **1,** 110–111 (2004).
26. M. Cohen, F. Roy, D. Hrault, Y. Cazaux, A. Gandolfi, J. Reynard, C. Cowache, E. Bruno, T. Girault, J. Vaillant, F. Barbier, Y. Sanchez, N. Hotellier, O. LeBorgne, C. Augier, A. Inard, T. Jagueneau, C. Zinck, J. Michailos, and E. Mazaleyrat, "Fully optimized Cu based process with dedicated cavity etch for 1.75 m and 1.45 m pixel pitch CMOS image sensor," in *IEEE International Electron Devices Meeting* (2006).
27. J. Herrmann, "Cross coupling and aliasing in modal wavefrontestimation," J. Opt. Soc. Am. **71,** 989–992 (1981).
28. F. J. Rigaut, J.–P. Veran, and O. Lai, "Analytical model forShack–Hartmann-based adaptive optics systems," Proc. SPIE **3353,** 1038–1048 (1998).
29. L. A. Poyneer and B. Macintosh, "Spatially filtered wavefrontsensor for high-order adaptive optics," J. Opt. Soc. Am. A **21,** 810–819 (2004).
30. M. A. van Dam, "Measuring the centroid gain of a Shack–Hartmann quad-cell wavefront sensor by using slope discrepancy," J. Opt. Soc. Am. A **22,** 1509–1514 (2005).
31. R. G. Lane, A. Glindemann, and J. C. Dainty, "Simulation of aKolmogorov phase screen," Waves Random Media **2,** 209–224 (1992).